Joule

CellPress

Article

Breathing-Mimicking Electrocatalysis for Oxygen Evolution and Reduction

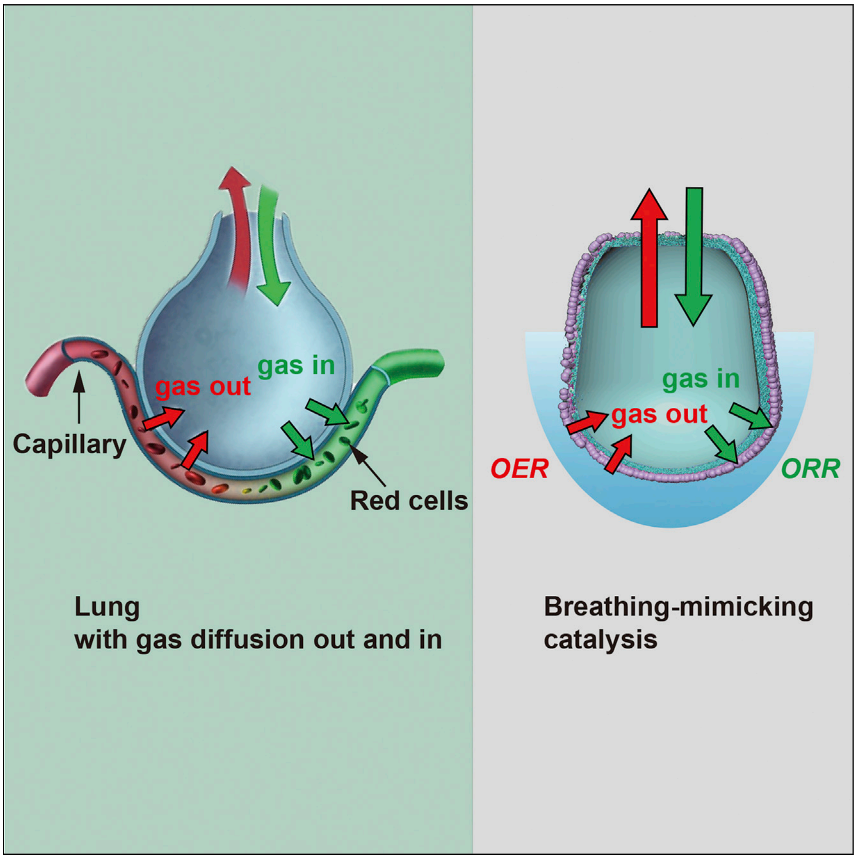

Inspired by the breathing process of mammalian alveoli, we developed a breathing-mimicking, pouch-type, nanoporous polyethylene (PE) structure for two-way efficient gas transport from and to the electrocatalyst/electrolyte interface. For OER, O_2 molecules are formed on the surface of the catalyst followed by fast O_2 diffusion through the nanoporous PE membrane into the gas phase inside the pouch. For ORR, the O_2 gas quickly diffuses through the PE membrane nanopores to the gas-liquid-solid three-phase contact reaction interface.

Jun Li, Yangying Zhu, Wei Chen, ..., Zewen Zhang, Steven Chu, Yi Cui

yicui@stanford.edu

HIGHLIGHTS

The electrode design mimics the essence of the mammalian two-way breathing pattern

Ample gas-liquid-solid three-phase contacts are achieved with a small catalyst loading

Newly formed O_2 in OER can diffuse to gas phase without bubble formation energy

O_2 gas reactant in ORR can be quickly delivered to the catalyst/electrolyte interface

Li et al., Joule 3, 557–569
February 20, 2019 © 2018 Published by Elsevier Inc.
https://doi.org/10.1016/j.joule.2018.11.015

Joule

CellPress

Article

Breathing-Mimicking Electrocatalysis for Oxygen Evolution and Reduction

Jun Li,[1,2] Yangying Zhu,[1] Wei Chen,[1] Zhiyi Lu,[1] Jinwei Xu,[1] Allen Pei,[1] Yucan Peng,[1] Xueli Zheng,[1] Zewen Zhang,[1] Steven Chu,[3,4] and Yi Cui[1,5,6,*]

SUMMARY

Electrocatalytic oxygen evolution and reduction reactions play a central role in clean energy technologies. Despite recent efforts to achieve fast gas reactant delivery to the reaction interface, efficient gas product evolution from the catalyst/electrolyte interface remains challenging. Inspired by the mammalian breathing process, here we developed an efficient electrocatalytic system to enable ample gas-solid-liquid three-phase contact lines and bidirectional gas pathways for evolution and consumption. During the oxygen evolution reaction, the newly formed O_2 molecules quickly diffuse to the gas phase, waiving the bubble formation energy in the electrolyte. A record low overpotential of 190 mV at 10 $mA \cdot cm^{-2}$ was achieved using Au/$NiFeO_x$ catalysts. During the oxygen reduction reaction, O_2 gas can transport to the catalyst/electrolyte interface, overcoming low O_2 solubility in water and leading to ~25-fold higher current densities for Ag/Pt bilayer nanoparticle catalysts. This breathing-mimicking design demonstrates efficient three-phase catalysis with a minimal catalyst thickness.

Context & Scale

The critical crisis of fossil fuel usage and emission has been driving the development of clean energy technologies, such as hydrogen production from water splitting and fuel cells to produce electricity. The optimization of both technologies should rely not only on rational realization of electrocatalyst compositions and structures but also on the efficient gas delivery from and to the catalyst surface. In this work, to mimic the mammalian alveoli with two-way breathing process, we demonstrate a pouch-type catalytic system for (1) efficient gas product evolution from and (2) gas reactant delivery to the catalyst surface, corresponding to oxygen evolution and reduction reactions, respectively. This design enables outstanding electrocatalytic performances with ample gas-liquid-solid three-phase contact interfaces and a small sub-100-nm catalyst thickness.

INTRODUCTION

Excessive fossil fuel emission has led to substantial risks and increasing concerns of global climate change in the past several decades. The research community has been motivated to develop and improve a variety of sustainable energy technologies such as electrochemical water splitting,[1,2] fuel cells,[3,4] and metal-air batteries.[5,6] Two key processes with these technologies are the oxygen evolution reaction (OER)[7,8] and the oxygen reduction reaction (ORR),[9,10] which are both kinetically sluggish and require the development of efficient electrocatalytic systems. Despite the predominant efforts in recent years toward optimizing catalyst compositions and structures,[1,4,11,12] a fundamental electrode design paradigm is still inadequate in enabling efficient mass transport and improving overall catalytic performances.[13]

Conventionally, gas is dissolved in the electrolyte and reaction takes place in the solid-liquid two-phase interface. Under standard pressure and temperature, the solubility of O_2 gas in water is as low as 70 mg O_2 per liter of water,[14] corresponding to a difference of 4–5 orders of magnitude fewer O_2 molecules than water molecules. Thus, the inefficient gas mass transport severely limits the electrocatalytic activity. To create three-phase contact lines, in the fuel cell community porous carbon supports are conventionally used as gas-diffusion layers (GDLs)[15–20] or floating electrodes[17] to deliver gas to the catalyst surface. However, the durability and degradation of these carbon-based GDLs due to the excessive water-induced electrode flooding[21] are long-standing issues that eventually impede mass transport and two-phase flow. On the other hand, as the reverse reaction of ORR, the OER overpotential and charge transfer are also strongly correlated with the gas transport limit but have seldom been addressed, particularly in the energy cost associated with the bubble formation. Previous studies reported that the micro-/nanoscale structures in electrode surface were beneficial to facilitate the gas bubble release and avoid the pinning of large bubbles at the electrode surface.[22,23] However, extra energy is still needed for the newly produced O_2 molecules to form bubbles and release into the electrolyte regardless of the bubble size,[24,25] thus constituting the bottleneck that prevents further decrease in the overpotential. Therefore, it is critical but highly challenging to develop an efficient mechanism for gas production and diffusion for OER without resorting to bubble formation.

The mammalian breathing process features one of the most sophisticated, nature-designed systems for two-way gas exchange patterns. Air is inhaled through bronchioles and directed to the alveoli where gas exchange between the bloodstream and lungs occurs (Figure 1A).[26] Encompassed by several thin epithelial cell layers of only a few microns, an alveolus membrane enables two-way gas diffusion into and out of the bloodstream while remaining impenetrable to the liquid (Figure 1B).[26] Furthermore, instead of plainly being a conventional gas-diffusion layer, the inner surface of alveoli is covered by a layer of lecithin-type molecules to reduce surface tension at the gas interface, while the outer membrane surface remains hydrophilic to closely contact the bloodstream. This micron-thick membrane endowed with asymmetric hydrophilicity/hydrophobicity can expedite gas evolution directly toward the gas phase inside an alveolus without forming unnecessary (and harmful) bubbles in the bloodstream. This exhaling process of the alveolus structure is also a highly energy-efficient scenario, as it eliminates the need to form bubbles inside a liquid environment that requires energy.[27,28]

Inspired by nature's ingenious structure, we herein demonstrate a breathing-mimicking electrocatalytic design for both directions of gas product evolution from the catalyst surface and gas reactant delivery to the catalyst surface, corresponding to OER and ORR, respectively (Figure 1C). The key design criteria to realize such a system requires (1) efficient mass transport for gas delivery and release, (2) ample three-phase contact regions for electrocatalytic reactions, and (3) robust hydrophobicity that can last for substantially longer time than conventional GDLs under electrochemical working conditions. Hence, we demonstrate a new electrode structure based on a 12-μm ultrathin nanoporous membrane made of polyethylene (PE), which is ~30-fold thinner than the conventional gas-diffusion electrode (i.e. polytetrafluoroethylene-coated porous carbon, Toray TGP-H-060, ~400 μm). The pores are densely packed to provide ample three-phase contact lines for more catalytic sites while retaining a reasonably low gas-diffusion resistance. One side of the PE membrane is first deposited with a layer of catalysts that also serves as a charge-transport layer and a hydrophilic surface coating. The catalyst-coated PE membrane is then rolled and sealed into a pouch structure mimicking an alveolus, designated as alveolus-like PE (alv-PE), with the gas phase inside and the liquid phase outside the alv-PE, respectively. The hydrophobic nature of the PE membrane prevents water from wetting into the pores.[29,30] The formation of the gas-liquid-solid three-phase contact lines on the catalyst-coated alv-PE surface enables fast transport of both gas molecules and charges. The alveolus-like PE structure creates a barrier impenetrable to water but accessible to two-way gas transport. For OER (similar to the exhaling process), the newly produced oxygen molecules from water splitting can efficiently diffuse from the catalyst/electrolyte interface toward the gas phase, without the additional energy cost of bubble formation (Figure 1D, left). For ORR (similar to the inhaling process), oxygen molecule reactants can be efficiently

[1]Department of Materials Science and Engineering, Stanford University, Stanford, CA 94305, USA

[2]Department of Chemistry, Stanford University, Stanford, CA 94305, USA

[3]Department of Physics, Stanford University, Stanford, CA 94305, USA

[4]Department of Molecular and Cellular Physiology, Stanford University, Stanford, CA 94305, USA

[5]Stanford Institute for Materials and Energy Sciences, SLAC National Accelerator Laboratory, 2575 Sand Hill Road, Menlo Park, CA 94025, USA

[6]Lead Contact

*Correspondence: yicui@stanford.edu

https://doi.org/10.1016/j.joule.2018.11.015

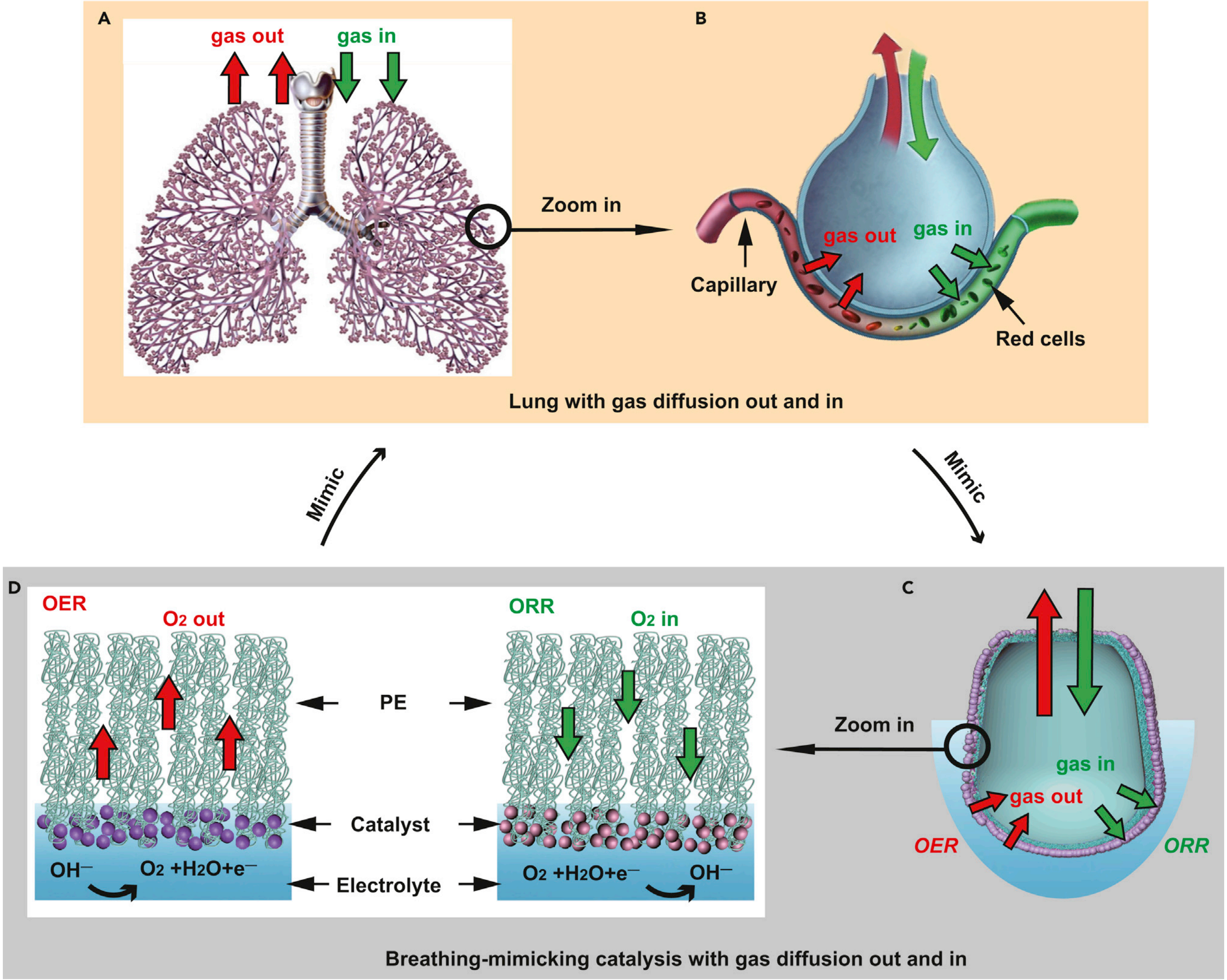

Figure 1. Illustration of the Breathing-Mimicking Structure for Electrocatalytic Oxygen Evolution and Reduction Reactions

(A and B) Schematic of a human lung, bronchial connection with alveoli (A), and a single alveolus (B). The red arrows indicate the outward diffusion of gas, and the green arrows indicate the inward diffusion of gas.

(C) Schematic of an artificial alveolus for dual functions of rapid gas delivery from and to the catalyst surface, corresponding to OER and ORR, respectively.

(D) Zoom-in schematic of an artificial alveolus. For OER, O_2 molecules are formed on the surface of the catalyst followed by fast O_2 diffusion through the PE membrane into the gas phase inside the pouch. For ORR, the O_2 gas is delivered into the pouch and diffuses through the PE membrane pores to the reaction three-phase contact lines.

delivered from the gas phase to the electrochemical reaction interfaces without predissolving into the bulk of the electrolyte (Figure 1D, right), thus leading to outstanding electrocatalytic performances on both oxygen-involved reactions. The ORR current density of -250 mA•cm^{-2} at 0.6 V was achieved with a Ag/Pt bilayer catalyst-coated alv-PE structure (all the potentials reported in this work were versus reversible hydrogen electrode [RHE]), which was ~25-fold higher than the same catalyst-loaded flat-PE structure. More strikingly, with a Au/NiFeO$_x$ catalyst-coated alv-PE structure for OER, a record low overpotential of 190 mV at 10 mA•cm^{-2} without iR correction was achieved, which was over 90 mV lower than the same catalyst-loaded flat or thicker PE membranes and even the carbon GDL-based electrodes.

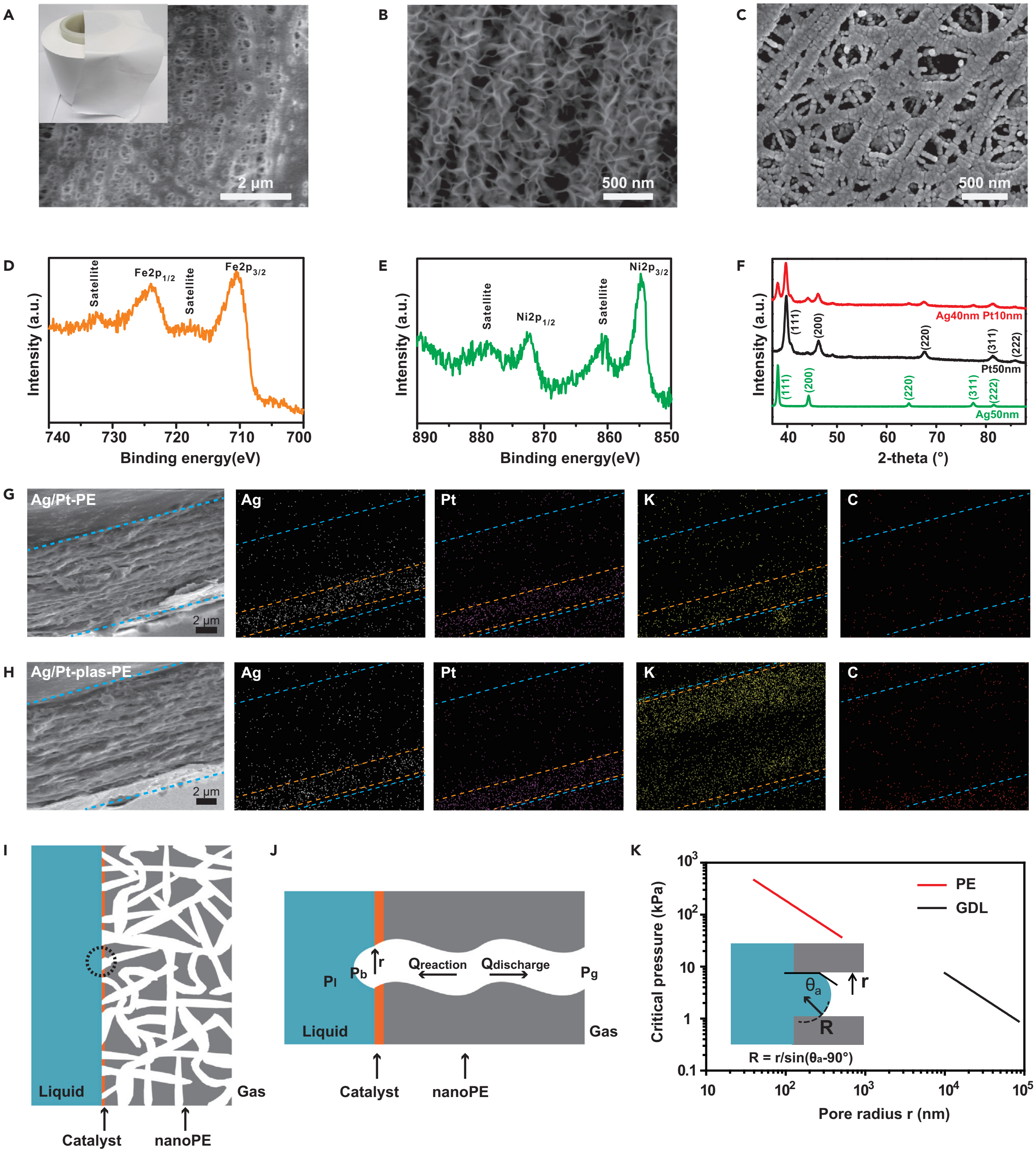

Figure 2. Structural Characterizations of the Catalyst-Coated PE Membranes

(A) SEM image of a pristine nanoporous PE membrane. Inset: a photograph of a pristine PE membrane roll.

(B) SEM image of a Au/NiFeO$_x$-coated PE membrane.

(C) SEM image of a Ag/Pt bilayer-coated PE membrane.

(D and E) XPS spectra of (D) Fe and (E) Ni of the Au/NiFeO$_x$-coated PE membrane.

(F) XRD patterns of Ag/Pt bilayer (red curve), Pt layer (black curve), and Ag layer (green curve) on PE membranes. The total metal thickness of each sample was ~50 nm.

Figure 2. ***Continued***

(G and H) SEM images and corresponding EDX mappings of the cross-section of (G) a Ag/Pt alv-PE membrane and (H) a plasma-treated Ag/Pt alv-PE membrane after 24 hr electrochemical test in a K^+-containing electrolyte. The high-density dotted area (between two marked orange dashed lines) shows the location of the Ag, Pt, and K elements, whereas the sparsely distributed dots (between two marked blue dash lines) are noise signal.

(I) Schematic of three-phase electrocatalysis with irregular-pore membrane for gas diffusion.

(J) Zoom-in image (dotted line in I) of a bubble embryo with pressure P_b in the electrolyte liquid environment with pressure P_l. On the other side of the membrane is bulk oxygen gas with pressure P_g. Electrocatalytic reaction generates gas into the embryo, while the high pressure of the bubble embryo drives a gas flow along the pore of the membrane to the bulk gas phase.

(K) Calculation result showing the critical burst-through pressure as a function of the pore radius for PE and carbon GDL. Inset: liquid-vapor interface advancing inside the pore with an advancing contact angle θ_a greater than 90°.

See also Figures S1–S6 and Appendix 1.

RESULTS

Structural Characterizations

The PE membranes consisted of interconnected nanofibers with a variety of pore sizes ranging from 80 to 1,000 nm (Figure 2A and inset). The electrocatalysts were deposited onto the PE membrane to maximize the electrochemical reaction kinetics without compromising the rates of gas transfer. $NiFeO_x$ and Pt were selected as typical and commonly used OER and ORR catalysts, respectively. Although nanoPE is an insulated material, the deposition of a thin-layer of metal or graphitic carbon can help nanoPE achieve excellent conductivity. Au and Ag were chosen as conductive layers. The OER electrode was fabricated by magnetron sputtering of 15 nm Au on PE membranes (Figure S1, details in Supplemental Experimental Procedures), followed by electrodeposition of a layer of $NiFeO_x$ (Figures 2B and S1, details in Supplemental Experimental Procedures). Energy-dispersive X-ray (EDX) elemental mapping (Figure S2) showed that Au, Ni, and Fe were deposited uniformly across the PE membrane. High-resolution X-ray photoelectron spectroscopy (XPS) for the Ni 2p and Fe 2p regions of the as-deposited Au/$NiFeO_x$ layer were measured (Figures 2D and 2E). The Ni $2p_{3/2}$ peak at 854.8 eV and Fe $2p_{3/2}$ peak at 710.9 eV were indicative of Ni^{2+} and Fe^{3+}, respectively, suggesting the formation of Au/$NiFeO_x$.[31,32] Similarly, the ORR electrode was formed by sequential deposition of 40 nm Ag and 10 nm Pt by magnetron sputtering (details in Supplemental Experimental Procedures). The membrane surface was covered by a layer of metal particles with average particle sizes of ~20 nm, while the pores remained open (Figures 2C and S3). The crystal structures of the surface metal layers were characterized by X-ray diffraction (XRD) (Figure 2F), confirming the face-centered-cubic structures of Ag and Pt on the surface. EDX spectroscopy elemental mapping (Figure S4) showed that both Ag and Pt were deposited uniformly across the entire PE membrane.

The merits of the PE membrane in resisting water flooding were first demonstrated and compared with a conventional carbon-based GDLs. The EDX mapping characterization of a AgPt-coated alv-PE membrane after 24 hr of electrochemical testing under 0.6 V in a K^+-containing electrolyte showed that the electrolyte only wet the same depth as the Ag and Pt layer thickness (Figure 2G), whereas K^+ penetrated through the whole thickness of a plasma-treated, hydrophilic alv-PE (Figure 2H) and a AgPt-coated GDL under similar conditions (Figure S5), suggesting the robustness of the gas-liquid-solid three-phase alv-PE structure after long-term use.

To prove that the formation of bubble did not occur on our OER interface, we conducted calculations from a pressure-driven-flow perspective.[33] The prerequisite for a gas embryo to grow in volume are: (1) the rate of gas generated by gas evolution reaction ($Q_{reaction}$) needs to be higher than the rate of gas discharged ($Q_{discharge}$) across the membrane (Figures 2I and 2J); and (2) the pressure of the gas embryo needs to overcome a critical pressure barrier. For a hydrophilic surface (i.e., the PE surface coated with catalysts in our work), this critical pressure corresponds to the maximum capillary pressure with a radius of curvature equal to the pore size of the membrane surface (Figure 2J). To satisfy both requirements, if, for example, a bubble can grow to a critical size (radius r = the pore radius of the membrane), in order for the size of the bubble to be sustained and continue growing, the gas generation rate by electrocatalysis needs to be three orders of magnitude higher than in our experiment to compensate for the gas discharge rate across the membrane (see Appendix 1 in Supplemental Information for detailed calculations). Thus, it is more favorable for the gas generated to directly transport across the alv-PE membrane toward the gas phase instead of growing a gas embryo into a macroscopic bubble.

The surface hydrophilicity was measured by a standard contact angle test (Figure S6). The pristine PE membrane clearly exhibited a hydrophobic nature with a contact angle of 105°. After coating with Ag/Pt and Au/$NiFeO_x$, the contact angles were reduced to 65° and 58°, respectively, suggesting the gradual conversion to a hydrophilic feature on the catalyst-coated side. Furthermore, when the whole PE membrane was treated by plasma, the contact angle was further reduced to 45°, indicating a good hydrophilic nature.

OER Electrocatalytic Activities

To assess the impact of the electrode structure on the electrochemical performance, we first compared the capability of the alv-PE structure for OER (Figure 3A) with that of the carbon-based GDL and flat-PE. The electrochemical impedances were first tested for OER and showed good conductivity (Figure S7). In the conventional electrochemical test configuration where a flat-PE membrane coated with the catalyst was placed inside 1 M KOH (Figure S8), the potential for achieving 10 $mA \cdot cm^{-2}$ current density was ~1.51 V (Figure 3B, purple curve), corresponding to an overpotential of 280 mV. Bubbles were observed from the onset potential and gradually increased at higher overpotentials (Figure 3B [purple arrow] and Video S1). This phenomenon was conventionally observed in many previous studies.[22,23,34] Both the catalyst-coated PE membrane and carbon GDL were then rolled and sealed into a pouch structure (designated alv-PE and alv-carbon GDL, respectively) and measured, whereby the outer membrane was in contact with the electrolyte and the inside pouch was left dry (Figure 3A). The alv-carbon GDL showed 10 $mA \cdot cm^{-2}$ current density at a reduced potential of ~1.46 V (corresponding to the 230 mV overpotential, Figure 3B [blue curve and arrow]). The alv-PE structure exhibited an even more reduced overpotential and higher current density (Figure 3B, red curve). The applied potential for the 10 $mA \cdot cm^{-2}$ current density was decreased to 1.42 V, corresponding to only 190 mV overpotential.

The OER electrochemical active area normalized current densities showed similar trends among the samples (Figure S9). Interestingly, despite its higher current density compared with the flat-PE and alv-carbon GDL counterparts, the alv-PE structure barely produced apparent bubbles from the catalyst surface until the applied voltage was increased to 1.65 V (Figure 3B [red arrow] and Video S2). The voltage gap between the onset potentials for OER and the bubble formation indicated that O_2 preferentially diffused toward the gas phase inside the pouch, instead of forming bubbles toward the electrolyte outside the pouch. The clearly reduced overpotential (from 1.51 to 1.42 V for 10 $mA \cdot cm^{-2}$ current density) was attributed to the waived bubble formation energy, which in turn increased its OER efficiency. Moreover, without the formed bubble blocking the electrolyte diffusion to catalyst

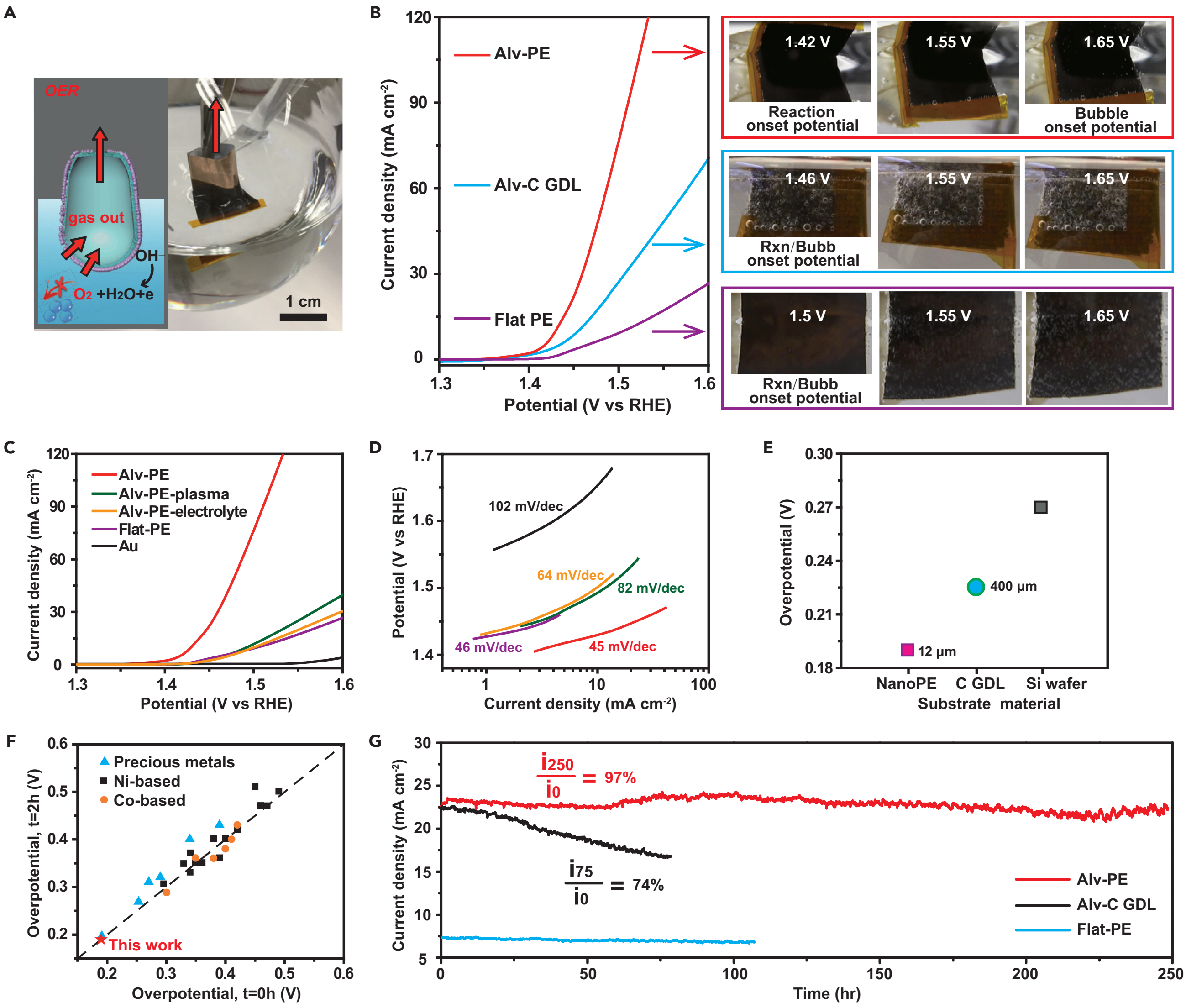

Figure 3. Electrocatalytic OER Using a Breathing-Mimicking Design

(A) Schematic and photograph of an alv-PE structure for OER. Inside and outside the alv-PE were the gas and liquid phases, respectively.

(B) LSV curves of Au/NiFeO$_x$-coated membranes with different structures: alv-PE (red curve), alv-carbon GDL (blue curve), and flat-PE (purple curve). Arrows indicate photographs of surfaces in each structure with O$_2$ bubbles onset potential.

(C) LSV curves of Au/NiFeO$_x$-coated PE membranes: alv-PE (red curve), flat-PE (purple curve), alv-PE pretreated by plasma (green curve), and alv-PE with electrolyte on both sides (orange curve). A PE membrane only coated with Au was also tested as a comparison (black curve).

(D) The corresponding Tafel plots calculated from (C).

(E) Overpotentials of 12-µm-thick PE membrane, 400-µm-thick carbon GDL, and Si wafer.

(F) A comparison of this work with other previously reported OER systems (Zhang et al.[8] and Ng et al.[31]) at 10 mA•cm^{-2}.

(G) Time-dependence OER current density stability of a Au/NiFeO$_x$-coated alv-PE (red curve), an alv-carbon GDL (black curve), and a flat-PE (blue curve), respectively.

See also Figures S7–S14 and Appendix 2.

surface, the catalytic active sites had more access to the reaction contact interface. In comparison, the hydrophilic treatment of the alv-PE with plasma or adding electrolyte to the inner pouch resulted in clear increase of overpotential and decrease of OER current densities (Figure 3C). Furthermore, the catalyst-coated alv-PE structure presented the smallest Tafel slope of 45 mV•dec^{-1} (Figure 3D) among these samples, suggesting fast charge transfer on the electrolyte-catalyst surface.

To evaluate the influence of different substrates on OER activity, we further investigated the overpotentials to reach 10 mA•cm^{-2} and compared them with carbon GDL and Si wafer (Figures 3E and S10). With the same catalyst loading and alv-PE structure, the alv-carbon GDL with the thickness of ~400 μm showed inferior performance to the 12-μm-thick alv-PE (Figure S11). The reduced performance of the GDL with a greater thickness can be ascribed to its ~42-fold lower critical burst-through pressure ΔPc (i.e., the minimum pressure difference between the liquid and the gas for the liquid to enter the pores) than that of the PE (Figure 2K) (see Appendix 2 in Supplemental Information for detailed calculations).[35] This lower critical burst-through pressure can result in water penetration and the discontinuous gas-delivery path, thus requiring additional gas bubble formation energy to transport O_2 molecules from the OER interface toward the liquid phase. However, in our catalyst-coated alv-PE structure with 12-μm thickness, the critical burst-through pressure was high enough to resist the water penetration into the membrane. Thus, the continuous gas pathway to the gas-liquid-solid interface enabled the direct transfer of newly formed O_2 molecules into the gas phase, and significantly lowered its overpotentials.

The chemical composition of the $NiFeO_x$ catalyst layer was then optimized by using different combinations of Ni(II) and Fe(II) ions in the precursor solutions for electrodeposition. Under our deposition conditions, the sample providing the best OER activity had a precursor ratio of Ni/Fe of 1:1 (Figure S12). Inductively coupled plasma mass spectrometry (ICP-MS) indicated that the actual atomic ratio of Ni/Fe in this catalyst was ~3:5. The thickness of the overall Au/$NiFeO_x$ catalyst film was then tuned either for the Au layer thickness via the sputtering time (Figure S13) or the $NiFeO_x$ layer thickness via different electrodeposition charges (Figure S14). In both cases, the increase of catalyst film thickness first led to the OER activity enhancement, while further increase of the film thickness decreased its OER activity. The corresponding scanning electron microscopy (SEM) images also indicated that the decrease of the catalytic activity was attributed to the blockage of nanopores on PE membranes (Figures 2B and S14), which impeded gas diffusion inside the pouch and subsequently required extra bubble nucleation energy.

The performance of Au/$NiFeO_x$ was further compared with recently reported state-of-the-art OER catalysts (Figure 3F).[8,31] The initial activity of each film was plotted versus its activity after 2 hr of continuous OER at 10 mA•cm^{-2}. Previously benchmarked OER catalysts were categorized into three groups based on their compositions, namely Ni-based, Co-based, and precious-metal-based. The Au/$NiFeO_x$-coated alv-PE structure presented the smallest overpotential of 190 mV at 10 mA•cm^{-2} without iR correction, similar to the previously reported best result on gelled FeCoW oxyhydroxides (with an overpotential of 191 mV) on a geometric surface area basis.[8]

The electrochemical stability of the Au/$NiFeO_x$-coated alv-PE was demonstrated by continuously running the OER measurement under a potential of 1.45 V versus RHE for 250 hr (Figure 3G), and compared with the alv-carbon GDL and flat-PE structures under identical conditions (except for the higher applied potential as 1.49 V). The current density of the Au/$NiFeO_x$-coated alv-PE was almost retained over 22 mA•cm^{-2} with ~97% activity retention during the entire 250-hr testing period, indicating its exceptional stability. In contrast, the current density of the alv-carbon GDL decayed to <74% activity retention after only 75 hr due to the flooding of the carbon GDL over long-term use. The flat-PE was stable over 110 hr with a low current activity of ~7.4 mA•cm^{-2}. This much enhanced electrochemical stability of the

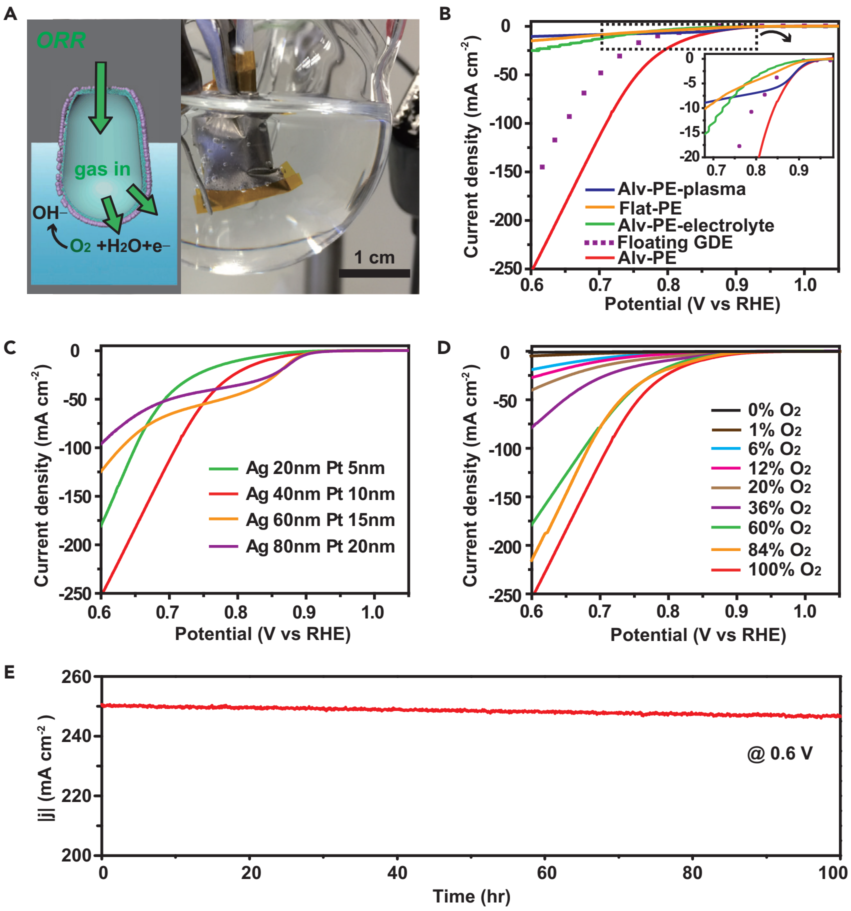

Figure 4. Electrocatalytic ORR Using a Breathing-Mimicking Design

(A) Schematic and photograph of an alv-PE structure for ORR. Inside and outside the alv-PE were the gas and liquid phases, respectively.

(B) LSV curves of a Ag/Pt bilayer-coated PE membrane (Ag 40 nm, Pt 10 nm) with different structures: alv-PE (red curve), flat-PE (orange curve), alv-PE pretreated by plasma (blue curve), and alv-PE with electrolyte on both sides (green curve). The dotted curve was plotted for comparison from Zalitis et al.[17]

(C) LSV curves of Ag/Pt alv-PE structure with different metal thickness as indicated.

(D) LSV curves of Ag/Pt alv-PE structure (Ag 40 nm, Pt 10 nm) with different O_2 concentrations (in Ar) supplied into the pouch.

(E) Time-dependence ORR current density (absolute value) of a Ag/Pt-coated alv-PE membrane at 0.6 V. See also Figures S15–S21 and Table S1.

alv-PE structure can be also attributed to its nanoporous and polymer features that are better designed than conventional carbon-based GDLs.

ORR Electrocatalytic Activities

For ORR, the alv-PE structure can deliver O_2 molecules to the three-phase reaction contact lines. Although the gas transport direction was similar to a conventional carbon-based GDL, the alv-PE showed higher activity and stability than the GDL. The ORR activity was investigated in a standard three-electrode system in an O_2-saturated 1 M KOH electrolyte. One piece of the flat Ag/Pt-coated PE membrane was rolled and sealed into a closed pouch-type structure (i.e., alv-PE) with one inlet for the O_2 gas to flow in (Figure 4A). The electrochemical impedances were first tested for ORR and showed good conductivity (Figure S15). The linear sweep voltammetry (LSV) curve of the alv-PE presented an onset potential of 0.90 V, and its current density continued to increase to a much higher level without being saturated. For example, when the applied voltage was 0.6 V, the ORR current density reached ~ -250 mA•cm^{-2} (Figure 4B, red curve). Even compared with a floating gas-diffusion electrode in previous studies[17] (Figure 4B, dotted curve), the alv-PE showed higher current density. In contrast, the flat-PE only showed -10 mA•cm^{-2} at 0.6 V (Figure 4B, orange curve) and exhibited a clear plateau of limited current density typically observed in diffusion-limited ORR measurements.[36,37] Furthermore, with either the plasma hydrophilic treatment (Figure 4B, purple curve) or the addition of the electrolyte into the alv-PE compartment (Figure 4B, green curve), the current density dropped to almost the same level as the flat-PE. The ORR electrochemical active area normalized current densities showed similar trends among the samples (Figure S16). When similar Ag/Pt bilayer catalysts were sputtered onto a flat Si substrate or flat GDL, the current density and onset voltages were even lower than those of a flat-PE (Figure S17). The difference in activity was attributed to the nanoporous and strongly hydrophobic nature of the PE membrane, which enabled a high O_2 density inside the pouch structure. The electrolyte wet the Ag/Pt electrocatalyst surface but not the nanopores inside the PE, which allowed O_2 gas diffusing across the PE membrane to contact directly with the Ag/Pt layer and electrolyte, forming an array of robust and efficient gas-liquid-solid three-phase contact lines (AgPt/H_2O/O_2) for ORR. Nonetheless, a conventional flat structure surrounded by the electrolyte only utilized the O_2 dissolved in the electrolyte, which resulted in insufficient three-phase contact interfaces and subsequently lower activity (Figure S18). The Tafel slope of the Ag/Pt-coated alv-PE membrane was calculated to be 43 mV•dec^{-1}, which was significantly smaller than that of other samples (Figure S19), indicating efficient charge transfer on the catalyst-electrolyte interface.[38]

The ORR activity dependence on the alv-PE catalyst thickness was also investigated. When the alv-PE catalyst total thickness was increased from 25 to 100 nm by tuning the metal sputtering time, the ORR current density first reached a maximum of -250 mA•cm^{-2} at 0.6 V and then decreased to less than 100 mA•cm^{-2} with a limited current plateau (Figure 4C). SEM images of the metal-coated membranes showed that the current density decreased, and the limiting current appearance was correlated with the blockage of nanopores on PE membranes (Figure S20). This comparison clearly indicated that the efficient passage of O_2 through alv-PE nanopores was the origin of the significant increase of ORR activity, highlighting the importance of the breathing-mimicking approach of the alveolus structure for O_2 uptake.

The ORR activity dependence on the O_2 concentration was further demonstrated using a mixture of Ar and O_2 gases under the same total pressure and flow rate (1 atm and 5 sccm, respectively). The ORR current density clearly increased with the O_2 concentration and did not show saturation even at > 80% of O_2 (Figure 4D). Even at a very low O_2 concentration of 1% (in 1 atm of total pressure mixed with Ar), the ORR activity was still clearly measured (Figures 4D and S21).

The ORR activity of our alv-PE structure was also compared with other results using catalyst-loaded GDLs (Table S1)[17,38–40] based on three common figures of merit for ORR, i.e., the overpotential at 10 mA•cm^{-2}, the mass activity (MA) at 10 mA•cm^{-2} (corresponding approximately to the current density expected for a 10% efficient solar-to-fuel conversion device[31]), and the geometric current density at 0.6 V. The MA was defined as the current density achieved per mass of catalyst. With a minimal catalyst loading of 0.07 mg•cm^{-2}, our Ag/Pt-coated alv-PE structure exhibited the highest geometric current density and more than 3-fold higher MA (143 mA•mg^{-1}) than previously reported ORR catalysts with GDLs at similar overpotentials. The extremely high MA of our sample was attributed to the large surface area for metal catalyst deposition and sufficient three-phase contact lines enabled by the pouch-type PE membrane, which was beneficial for fast O_2 transport. The electrochemical stability of the Ag/Pt-coated alv-PE structure was tested by continuously running the ORR measurement under a potential of 0.6 V for 100 hr (Figure 4E). The current density (absolute value) was around 250 mA•cm^{-2} with ~98% activity retention, indicating the excellent stability of our catalyst on the alv-PE structure.

DISCUSSION

It was recently reported that nanoporous polyethylene membrane enabled an enhanced CO_2 delivery to the catalyst-electrolyte interface and a high faradaic efficiency of electroreduction to CO.[35] Nonetheless, similar to all the GDL-based electrodes, the opposite scenario of producing gas from the three-phase contact lines has not been realized previously. Indeed, the two-way breathing process of mammalian alveoli represents a highly efficient and unique gas-exchange system at the liquid-solid-gas contact lines in a dual-direction manner. In our work, this natural design concept is subtly mimicked for the electrocatalytic OER and ORR systems to realize the dual functions of rapid gas generation from and delivery to the electrochemical reaction interface, enabled by a catalyst-coated, nanoporous PE membrane in a pouch structure. Interestingly, our design can switch between a flat, conventional electrode structure surrounded by the electrolyte, and an alveolus-mimicking structure that separates liquid and gas phases. Such a unique feature enables a direct and unambiguous comparison of these two structures using the same catalyst. For a Au/$NiFeO_x$ OER catalyst, the alv-PE structure allows for the fast transport of newly produced O_2 molecules into an existing gas phase, waiving the energy cost of the bubble nucleation process. Thus, compared with the conventional flat electrode structures or a carbon-based GDL, the alv-PE structure exhibits a clear reduction of overpotential that is comparable with the best reported OER performances. For a Ag/Pt ORR catalyst, the alv-PE structure leads to a current density ~25-fold higher than that of a flat structure, which is attributed to the greatly increased available O_2 flux to the electrocatalytic gas-liquid-solid three-phase contact lines.

In addition to its high efficiency, the catalyst-coated alv-PE structure features an ultrathin layer of the catalyst. The typical thickness of the catalyst deposited on the PE membrane is around 50–100 nm, substantially thinner than most of the previously reported catalyst thicknesses (i.e., hundreds of nanometers to tens of microns). Thus, an extremely high MA is realized in our system, resulting in significant cost reduction for catalysts. The high efficiency with such a low catalyst loading is attributed to the unique structure of our membrane device, where the gas reactants and products are continuously delivered through the PE membrane to/from the gas-liquid-solid three-phase contact lines, thus enabling a full utilization of almost all the active sites of a catalyst. Moreover, our proposed design can be readily applied to many other multiphase catalytic systems. The catalysts can be conveniently tuned to fit for different electrochemical reactions. The PE membrane can also be replaced with other nanoporous, hydrophobic membranes with high temperature stability.

In summary, we have developed a breathing-mimicking two-way OER and ORR electrocatalytic system that exhibits the following features. (1) Pouch-type nanoporous, hydrophobic, 12-μm-thick PE membranes serve as the most important unit for catalyst deposition and function, corresponding to an artificial alveolus structure. (2) The OER mimics the exhaling process whereby the fast gas transport to the gas phase helps to eliminate the energy of O_2 gas formation and thus reduces the overpotential. (3) The ORR mimics the inhaling process whereby gas reactant is efficiently delivered to the gas-liquid-solid contact lines for enhanced catalytic reaction. (4) The nanoporous and polymer features of PE membranes exhibit a much more enhanced electrochemical stability than conventional carbon-based GDLs and can be loaded with a vast variety of electrocatalysts for different reactions. Coupled with state-of-the-art electrocatalysts, further exploration of the breathing-mimicking gas-liquid-solid three-phase electrode can offer more exciting opportunities for catalysis.

EXPERIMENTAL PROCEDURES

Details of all experimental procedures can be found in Supplemental Information.

SUPPLEMENTAL INFORMATION

Supplemental Information includes Supplemental Experimental Procedures, 2 appendices, 21 figures, 1 table, and 2 videos and can be found with this article online at https://doi.org/10.1016/j.joule.2018.11.015.

ACKNOWLEDGMENTS

This work was initiated by the support of the Department of Energy, Office of Basic Energy Sciences, Materials Sciences and Engineering Division, under contract DEAC02-76-SF00515. We also acknowledge the use and support of the Stanford Nano Shared Facilities and Stanford Nanofabrication Facility.

AUTHOR CONTRIBUTIONS

J.L., S.C., and Y.C. conceived the idea of the project. J.L., W.C., J.X., Y.P., and Z.Z. performed structural characterization. J.L., W.C., and Z.L. carried out device fabrication and performance measurements. J.L., Y.Z., and X.Z. made data analyses. J.L., S.C., and Y.C. wrote the manuscript with assistance from Y.Z. and A.P. S.C. and Y.C. supervised the whole project. All authors discussed the results and commented on the manuscript at all stages.

DECLARATION OF INTERESTS

The authors declare no competing interests.

Received: September 27, 2018
Revised: November 4, 2018
Accepted: November 20, 2018
Published: December 20, 2018

REFERENCES

1. Roger, I., Shipman, M.A., and Symes, M.D. (2017). Earth-abundant catalysts for electrochemical and photoelectrochemical water splitting. Nat. Rev. Chem. *1*, https://doi.org/10.1038/s41570-016-0003.
2. Li, J., and Zheng, G. (2017). One-dimensional earth-abundant nanomaterials for water-splitting electrocatalysts. Adv. Sci. (Weinh) *4*, 1600380.
3. Seh, Z.W., Kibsgaard, J., Dickens, C.F., Chorkendorff, I.B., Nørskov, J.K., and Jaramillo, T.F. (2017). Combining theory and experiment in electrocatalysis: insights into materials design. Science *355*, https://doi.org/10.1126/science.aad4998.
4. Yan, B., Concannon, N., Milshtein, J., Brushett, F., and Surendranath, Y. (2017). A membrane-free neutral pH formate fuel cell enabled by a selective nickel sulfide oxygen reduction catalyst. Angew. Chem. Int. Ed. *56*, 7496–7499.
5. Wang, Z.-L., Xu, D., Xu, J.-J., and Zhang, X.-B. (2014). Oxygen electrocatalysts in metal-air batteries: from aqueous to nonaqueous electrolytes. Chem. Soc. Rev. *43*, 7746–7786.
6. Shao, Y., Ding, F., Xiao, J., Zhang, J., Xu, W., Park, S., Zhang, J.G., Wang, Y., and Liu, J. (2013). Making Li-air batteries rechargeable: material challenges. Adv. Funct. Mater. *23*, 987–1004.
7. Li, J., Wang, Y., Zhou, T., Zhang, H., Sun, X., Tang, J., Zhang, L., Al-Enizi, A.M., Yang, Z., and Zheng, G. (2015). Nanoparticle superlattices as efficient bifunctional electrocatalysts for water splitting. J. Am. Chem. Soc. *137*, 14305–14312.
8. Zhang, B., Zheng, X., Voznyy, O., Comin, R., Bajdich, M., García-Melchor, M., Han, L., Xu, J.,

Liu, M., Zheng, L., et al. (2016). Homogeneously dispersed multimetal oxygen-evolving catalysts. Science *352*, 333–337.

9. Chen, C., Kang, Y., Huo, Z., Zhu, Z., Huang, W., Xin, H.L., Snyder, J.D., Li, D., Herron, J.A., Mavrikakis, M., et al. (2014). Highly crystalline multimetallic nanoframes with three-dimensional electrocatalytic surfaces. Science *343*, 1339–1343.
10. Wang, H., Xu, S., Tsai, C., Li, Y., Liu, C., Zhao, J., Liu, Y., Yuan, H., Abild-Pedersen, F., Prinz, F.B., et al. (2016). Direct and continuous strain control of catalysts with tunable battery electrode materials. Science *354*, 1031–1036.
11. Liu, C., Tang, J., Chen, H., Liu, B., and Yang, P. (2013). A fully integrated nanosystem of semiconductor nanowires for direct solar water splitting. Nano Lett. *13*, 2989–2992.
12. Kuang, M., Wang, Q., Ge, H., Han, P., Gu, Z., Al-Eniz, A.M., and Zheng, Z. (2017). $CuCoO_x$/FeOOH core-shell nanowires as an efficient bifunctional oxygen evolution and reduction catalyst. ACS Energy Lett. *2*, 2498–2505.
13. Tang, C., Wang, H., and Zhang, Q. (2018). Multiscale principles to boost reactivity in gas-involving energy electrocatalysis. Acc. Chem. Res. *51*, 881–889.
14. Speight, J.G. (2005). Lange's Handbook of Chemistry, *vol. 1* (McGraw-Hill).
15. Du, L., Shao, Y., Sun, J., Yin, G., Liu, J., and Wang, Y. (2016). Advanced catalyst supports for PEM fuel cell cathodes. Nano Energy *29*, 314–322.
16. Falkowski, J., Concannon, N., Yan, B., and Surendranath, Y. (2015). Heazlewoodite, Ni_3S_2: a potent catalyst for oxygen reduction to water under benign conditions. J. Am. Chem. Soc. *137*, 7978–7981.
17. Zalitis, C.M., Kramer, D., and Kucernak, A.R. (2013). Electrocatalytic performance of fuel cell reactions at low catalyst loading and high mass transport. Phys. Chem. Chem. Phys. *15*, 4329–4340.
18. Hao, G.P., Sahraie, N.R., Zhang, Q., Krause, S., Oschatz, M., Bachmatiuk, A., Strasser, P., and Kaskel, S. (2015). Hydrophilic non-precious metal nitrogen-doped carbon electrocatalysts for enhanced efficiency in oxygen reduction reaction. Chem. Commun. (Camb.) *51*, 17285–17288.
19. Zhang, G., Munoz, M., and Etzold, B. (2016). Accelerating oxygen-reduction catalysts through preventing poisoning with non-reactive species by using hydrophobic ionic liquids. Angew.Chem. Int. Ed. *55*, 2257–2261.
20. Seredych, M., Szczurek, A., Fierro, V., Celzard, A., and Bandosz, T.J. (2016). Electrochemical reduction of oxygen on hydrophobic ultramicroporous PolyHIPE carbon. ACS Catal. *6*, 5618–5628.
21. Park, J., Oh, H., Ha, T., Lee, Y.I., and Min, K. (2015). A review of the gas diffusion layer in proton exchange membrane fuel cells: durability and degradation. Appl. Energy *155*, 866–880.
22. Faber, M.S., Dziedzic, R., Lukowski, M.A., Kaiser, N.S., Ding, Q., and Jin, S. (2014). High-performance electrocatalysis using metallic cobalt pyrite (CoS_2) micro- and nanostructures. J. Am. Chem. Soc. *136*, 10053–10061.
23. Lu, Z., Zhu, W., Yu, X., Zhang, H., Li, Y., Sun, X., Wang, X., Wang, H., Wang, J., Luo, J., and Lei, X. (2014). Ultrahigh hydrogen evolution performance of under-water "superaerophobic" MoS_2 nanostructured electrodes. Adv. Mater. *26*, 2683–2687.
24. Jones, S.F., Evans, G.M., and Galvin, K.P. (1999). Bubble nucleation from gas cavities—a review. Adv. Colloid Interface Sci. *80*, 27–50.
25. Sakuma, G., Fukunaka, Y., and Matsushima, H. (2014). Nucleation and growth of electrolytic gas bubbles under microgravity. Int. J. Hydrogen Energy *39*, 7638–7645.
26. Weibel, E.R., Sapoval, B., and Filoche, M. (2005). Design of peripheral airways for efficient gas exchange. Resp. Physiol. Neurobiol. *148*, 3–21.
27. Sung, J.H., Esch, M.B., Prot, J.M., Long, C.J., Smith, A., Hickman, J.J., and Shuler, M.L. (2013). Microfabricated mammalian organ systems and their integration into models of whole animals and humans. Lab Chip *13*, 1201–1212.
28. Ionescu, C.M. (2013). The Human Respiratory System: An Analysis of the Interplay between Anatomy, Structure, Breathing and Fractal Dynamics (Springer), pp. 13–22.
29. Liu, K., Yao, X., and Jiang, L. (2010). Recent developments in bio-inspired special wettability. Chem. Soc. Rev. *39*, 3240–3255.
30. Liu, M., Zheng, Y., Zhai, J., and Jiang, L. (2009). Bioinspired super-antiwetting interfaces with special liquid-solid adhesion. Acc. Chem. Res. *43*, 368–377.
31. Ng, J.W.D., García-Melchor, M., Bajdich, M., Chakthranont, P., Kirk, C., Vojvodic, A., and Jaramillo, T.F. (2016). Gold-supported cerium-doped NiO_x catalysts for water oxidation. Nat. Energy *1*, 16053.
32. Yamashita, T., and Hayes, P. (2008). Analysis of XPS spectra of Fe^{2+} and Fe^{3+} ions in oxide materials. Appl. Surf. Sci. *254*, 2441–2449.
33. Klinkenberg, L.J. (1941). The Permeability of Porous Media to Liquids and Gases. Drilling and Production Practice (American Petroleum Institute).
34. Li, S., Wang, Y., Peng, S., Zhang, L., Al-Enizi, A.M., Zhang, H., Sun, X., and Zheng, G. (2016). Co-Ni-based nanotubes/nanosheets as efficient water splitting electrocatalysts. Adv. Energy Mater. *6*, 1501661.
35. Li, J., Chen, G., Zhu, Y., Liang, Z., Pei, A., Wu, C.L., Wang, H., Lee, H.R., Liu, K., Chu, S., and Cui, Y. (2018). Efficient electrocatalytic CO_2 reduction on a three-phase interface. Nat. Catal. *1*, 592–600.
36. Holewinski, A., Idrobo, J.-C., and Linic, S. (2014). High-performance Ag-Co alloy catalysts for electrochemical oxygen reduction. Nat. Chem. *6*, 828–834.
37. Zhang, L., Lee, K., and Zhang, J. (2007). The effect of heat treatment on nanoparticle size and ORR activity for carbon-supported Pd-Co alloy electrocatalysts. Electrochim. Acta *52*, 3088–3094.
38. Liang, Y., Li, Y., Wang, H., Zhou, J., Wang, J., Regier, T., and Dai, H. (2011). Co_3O_4 nanocrystals on graphene as a synergistic catalyst for oxygen reduction reaction. Nat. Mater. *10*, 780–786.
39. Liang, Y., Wang, H., Zhou, J., Li, Y., Wang, J., Regier, T., and Dai, H. (2012). Covalent hybrid of spinel manganese-cobalt oxide and graphene as advanced oxygen reduction electrocatalysts. J. Am. Chem. Soc. *134*, 3517–3523.
40. Lu, Z., Xu, W., Ma, J., Li, Y., Sun, X., and Jiang, L. (2016). Superaerophilic carbon-nanotube-array electrode for high-performance oxygen reduction reaction. Adv. Mater. *28*, 7155–7161.